Microstructural evolution and dynamic compressive properties of engineered cementitious composites at elevated temperatures

Meng Chen [a,b], Yuting Wang [a], Tong Zhang [a,*], Mingzhong Zhang [c,*]

[a] School of Resources and Civil Engineering, Northeastern University, Shenyang, 110819, China

[b] Institute for Frontier Technologies of Low-Carbon Steelmaking, Northeastern University, Shenyang, 110819, China

[c] Department of Civil, Environmental and Geomatic Engineering, University College London, London, WC1E 6BT, UK

Abstract: This paper presents a comprehensive study on the microstructural evolution and quasi-static and dynamic compressive properties of engineered cementitious composites (ECC) at elevated temperatures (20, 105, 250, 400, 600 and 800 °C). Split Hopkinson pressure bar (SHPB) was adopted to investigate the compressive behaviour of ECC at various strain rates after exposure to elevated temperatures, while the corresponding microstructural evolution was characterised using scanning electron microscopy (SEM), digital electron microscope and mercury intrusion porosimetry (MIP) along with fractal analysis. Results indicate that ECC exhibited strain rate effect and high temperature sensitivity simultaneously. The residual dynamic compressive strength of ECC increased by 33.0−50.4% with the rising strain rate from 79.8 to 127.1 s^{-1}. It reached the maximum value at 105 °C but reduced to 14.3−25.8% at 800 °C compared to that at 20 °C. The change in dynamic increase factor of ECC for various temperatures and strain rates can be well predicted using the developed equation. The thermal decomposition of PVA fibres was the main detrimental affecting the dynamic performance of ECC at sub-high temperatures (below 400 °C), whereas the negative effects caused by the formation of pores and microcracks in the matrix dominated at higher temperatures (400−800 °C). Microscopic damage induced by elevated temperatures aggravated the deterioration degree under dynamic compressive load, whilst the larger the difference in the macro/micro pore structural fractal dimension of 2.50/2.67, the greater the temperature softening effect on impact resistance of ECC.

Keywords: Strain hardening cementitious composites; Split Hopkinson pressure bar (SHPB); Microstructure; Dynamic increase factor; Fractal dimension

---

* Corresponding authors.

E-mail addresses: zhangtong@mail.neu.edu.cn (T. Zhang); mingzhong.zhang@ucl.ac.uk (M. Zhang)

1. Introduction

To overcome the brittleness of ordinary cementitious materials, engineered cementitious composites (ECC), a type of high-performance fibre reinforced cementitious composites, have been developed in last two decades based on micromechanics and fracture mechanics theory [1,2]. The tensile strain capacity of polyvinyl alcohol (PVA) fibre reinforced ECC can reach 3−5% along with desirable strain-hardening and multiple microcracking behaviour [3–5], which is over 300 times that of traditional cementitious composites [6,7]. The average crack width of ECC is only about 60 μm even if the tensile strain exceeds 1% [8]. Due to the fibre bridging effect and dispersing stress in concrete, ECC is mostly fractured with multiple microcracks under quasi-static tensile load [9,10], leading to a high ductility and fracture toughness suitable for different civil infrastructure applications [11]. The control of crack expansion can also reduce the chemical attacks of ECC, which in turn improves the durability and service life of concrete structures [12–14].

In recent years, a number of studies have been focused on the thermal and microstructural evolution of ECC with exposure temperature. Due to the low water-to-binder (w/b) ratio, the hydration process of ECC is relatively longer at ambient temperature. After exposure to 200 °C, the pozzolanic activity of binders (e.g., fly ash) is stimulated by thermal condition [11,15], which increases the content of calcium silicate hydrates (C–S–H) gels, resulting in denser microstructure. Meanwhile, gel particles are attracted to each other due to the free water evaporation [16–18]. The bonding of fibre and matrix is enhanced and the strain-hardening behaviour of PVA fibre reinforced ECC still maintains before 200 °C [10,19]. Around 250 °C, PVA fibres begin to melt but melted products are still remained, leading to the internal pore pressure developed due to the difficulty to deliver vapour [20–22]. Following this, the porosity of ECC at 400 °C increased due to the fibre disappearance and a relatively small amount of crack [23]. Then, a large number of internal cracks initiated and propagated over 400 °C, which can be attributed to the rapid decomposition of hydration products (e.g., C–S–H, calcium hydroxide and calcium carbonate) [24–26]. Besides, the thermal stress induced by large temperature gradients rises significantly [27]. Thus, the crystal microstructure is severely damaged and exhibits peeled and irregular loose features at 800 °C [28,29]. In general, the microstructure of ECC exposed to elevated temperatures can be improved prior to the melting of fibres and deteriorate rapidly afterwards.

So far, the role of strain rate in compressive properties of ECC has been increasingly studied. The strain rate is determined by the speed of dynamic loading. In accordance with loading speed, the loads

can be classified as seismic, impact and explosion, while the corresponding strain rate can reach up to 10^3 s^{-1} [30]. It is worth mentioning that cementitious materials usually exhibit an obvious strain rate effect that the dynamic properties are enhanced with increasing strain rate [31–34]. This can be ascribed to the combined effects of three aspects: (1) structural effects induced by lateral inertia and end friction limitation [35]; (2) Stefan effect due to free water movement as a hindrance to crack growth [36]; (3) microcrack development effect during the whole loading process [37]. The structural effects are only noticeable at strain rates above 200 s^{-1} because of the pre-treatment measures for tests [38], whereas the latter two aspects would play the essential influence on dynamic properties of ECC. The Stefan effect process is included in the microcrack propagation and the bonding of matrix and fibre mainly affects the development of microcracks [34,39,40]. Anyway, the slippage behaviour is best for fibre bridging cracks rather than the pull of weak bond and break of strong bond [41]. Thus, with the increase of stain rate, the number of microcracks increases and more fibres could resist or delay the crack growth effectively [42]. Although the dynamic behaviour of ECC at room temperature has been increasingly explored, the coupling effect of high temperature and dynamic loading on mechanical properties of ECC has been rarely addressed, which hinders its widespread applications.

The main purpose of this study is to provide a systematic and fundamental understanding of the quasi-static and dynamic compressive performance of PVA fibre reinforced ECC exposed to various temperatures (20, 105, 250, 400, 600 and 800 °C). A series of tests including ultrasonic pulse velocity (UPV) test, quasi-static compressive test and dynamic compressive test using split Hopkinson pressure bar (SHPB) under various strain rates (80−125 s^{-1}) were conducted to characterise the quasi-static and dynamic compressive strengths, dynamic increase factor (DIF) and energy absorption of ECC, with special focus on the effects of exposure temperature and strain rate on the compressive behaviour of ECC. Afterwards, scanning electron microscopy (SEM), digital microscope and mercury intrusion porosimetry (MIP) were adopted to explore the evolution of microstructure of ECC matrix and PVA fibre morphology across the crack interface in ECC at elevated temperatures. Based on the obtained experimental results, the damage mechanisms of ECC under high temperatures and dynamic compressive load were analysed and discussed in detail from both the microscopic and macroscopic points of view, with the assistance of fractal analysis.

2. Experimental program

2.1 Raw materials

P.I 42.5R Portland cement with specific gravity of 3.09 as per Chinese standard GB175−2007 [43]

and fly ash with specific gravity of 2.30 according to ASTM C618−17a [44] were used as binders, the chemical compositions of which are presented in Table 1. Silica sand was adopted as fine aggregate. The particle size distribution of binders and sand are shown in Fig. 1. To ensure the workability of the mixture, polycarboxylated polyether polymer (aqueous solutions) with pH of 6–7 was applied as the superplasticiser. PVA fibre (Kuraray Co., Ltd., Japan) is used in this study as reinforcement, the physical and mechanical properties of which are given in Table 2.

Table 1 Chemical compositions (wt%) of cement and fly ash.

Oxide	CaO	SiO_2	Al_2O_3	Fe_2O_3	SO_3	MgO	K_2O	TiO_2	Loss on Ignition
Cement	68.07	19.39	4.34	3.14	2.40	1.37	0.74	0.21	2.40
Fly ash	2.91	56.95	32.40	3.09	0.36	0.52	2.08	1.25	2.45

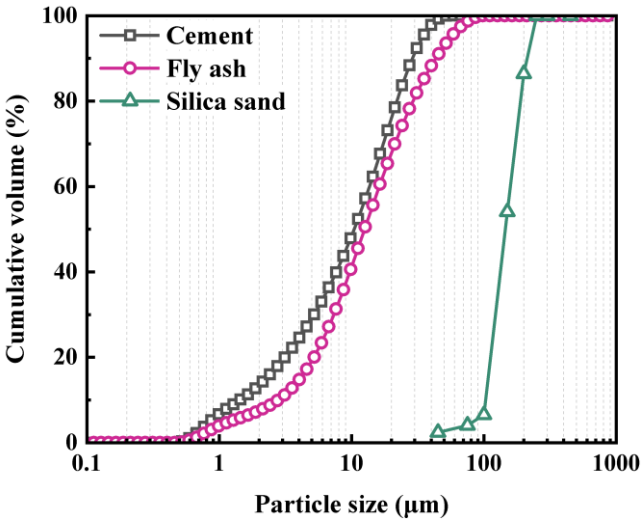

Fig. 1. Particle size distribution of cement, fly ash and silica sand.

Table 2 Properties of PVA fibre.

Diameter (μm)	Length (mm)	Density (kg/m^3)	Tensile strength (MPa)	Elastic modulus (GPa)	Melting point (°C)	Vaporisation point (°C)
40	12	1300	1560	41	248	439

2.2 Mix proportion

The mix proportion of ECC adopted in this study was kept consistent with that of ECC M45 used in Ref. [45], with w/b ratio of 0.27 and mass ratio of cement, fly ash, and silica sand of 1: 1.2: 0.8, as given in Table 3. The content of superplasticiser was kept as 0.4% of the sum of cement and fly ash by mass. The content of PVA fibre in this study was 2 % by volume [19].

Table 3 Mix proportion (kg/m^3) of ECC.

Cement	Fly ash	Silica sand	Water	Superplasticiser	PVA fibre
563	676	451	335	4.98	26

2.3 Sample preparation

The preparation process for all ECC specimens is illustrated in Fig. 2. The total mixing time for all mixtures was around 15 min. After the mixing process, the mixture was poured into moulds of different sizes of ⌀50 × 100 mm, ⌀100 × 200 mm and ⌀100 × 50 mm for the next UPV test, quasi-static compressive test and dynamic compressive test, respectively [46]. Table 4 summarises the experimental program in terms of number and size of specimens for each test. Finally, all specimens were demoulded after pouring for 1 d and then moved to the curing condition (20 ± 2 °C and 95% relative humidity) for 27 d.

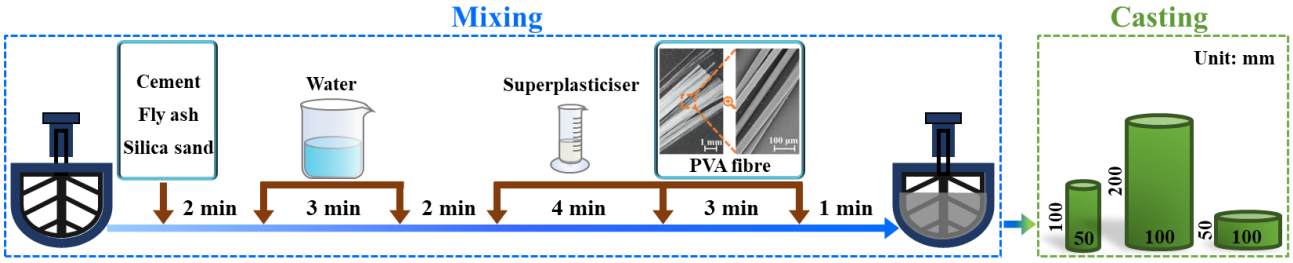

Fig. 2. Preparation of ECC specimens.

Table 4 Details for the tests of ECC at elevated temperatures.

Test	Specimen size (mm)	Specimen number	Temperature (°C)	Strain rate (s^{-1})
Ultrasonic pulse velocity	⌀50 × 100	6 (T) × 3 (R)	20, 105, 250, 400, 600, 800	–
Quasi-static compression	⌀100 × 200	6 (T) × 3 (R)	20, 105, 250, 400, 600, 800	8.33×10^{-5}
Dynamic compression	⌀100 × 50	6 (T) × 4 (S) × 3 (R)	20, 105, 250, 400, 600, 800	80, 95, 110, 125

Note: T – temperature, R – replication, S – strain rate.

2.4 Heating method

After curing for 28 d, the specimens were moved to ambient environment and dried before exposure to high temperature. To reach the different experimental temperatures (see Table 4), the heating rate was set as 10 °C/min in this study according to ASTM E831−14 [47]. When the target temperature was achieved, ECC specimens were kept at this temperature for 2 h and then naturally cooled down to ambient temperature in the furnace. The cooling process lasted for about 2–6 h.

2.5 Test methods

2.5.1 Ultrasonic pulse velocity test

To evaluate the integrity and quality of ECC after exposure to various temperatures, UPV tests were carried out on cylindrical specimens using an acoustic parameter tester (HS-YS403B). The input parameters of voltage, pulse width, bandwidth, and sampling rate were set as 250 V, 5000 ns, 10

kHz−1.5 MHz and 0.16 μs, respectively. A coupled gel was screeded to the ends of specimens and the transducers were contacted with them to measure the velocity.

2.5.2 Quasi-static compressive test

The 28 d quasi-static compressive strength was measured from the cylinder ECC specimens as per ASTM C469−14 [48]. The loading rate was set as 1.0 mm/min that approximately equals to the strain rate of 8.33×10^{-5} s^{-1} during the test process.

2.5.3 Dynamic compressive test

The dynamic compressive test on ECC after high-temperature treatment at various strain rates was carried out using a SHPB device with diameter of 100 mm, in consistence with the previous studies [49,50]. Moreover, high-strength steel materials are used to make the basic components of the SHPB testing system, as shown in Fig. 3. During the SHPB test, the incident bar was pushed by the striker bar through charging 0.4−1.0 MPa nitrogen into the gas chamber at different depths. Fig. 4 presents an example of stress equilibrium validation for test specimen. The sum of the incident stress and the reflected stress coincides well with the transmitted stress during the test, indicating that the specimen has achieved an environment of dynamic stress equilibrium [33,50]. Hence, the dynamic compressive properties of ECC after being exposed to different temperatures were measured by cylindrical specimens. On the basis of the elastic stress wave propagation theory, the changes in stress ($\sigma_s(t)$), strain ($\varepsilon_s(t)$) and strain rate ($\dot{\varepsilon}_s(t)$) are calculated as [51]:

$$\begin{cases} \sigma_s(t) = \dfrac{E_b A_b}{2 A_s} \left[\varepsilon_i(t) + \varepsilon_r(t) + \varepsilon_t(t)\right] \\ \varepsilon_s(t) = \dfrac{C_0}{l_s} \displaystyle\int_0^t \left[\varepsilon_i(t) - \varepsilon_r(t) - \varepsilon_t(t)\right] \mathrm{d}t \\ \dot{\varepsilon}_s(t) = \dfrac{C_0}{l_s} \left[\varepsilon_i(t) - \varepsilon_r(t) - \varepsilon_t(t)\right] \end{cases} \tag{1}$$

where $\varepsilon_i(t)$, $\varepsilon_r(t)$ and $\varepsilon_t(t)$ stand for the incident pulse, reflected pulse and transmission pulse, respectively, E_b and A_b denote the elastic modulus (MPa) and cross-sectional area (mm^2) of the bars, respectively, C_0 is the longitudinal wave velocity (m/s), and A_s and l_s are the cross-sectional area (mm^2) and initial thickness (mm) of the tested specimen, respectively.

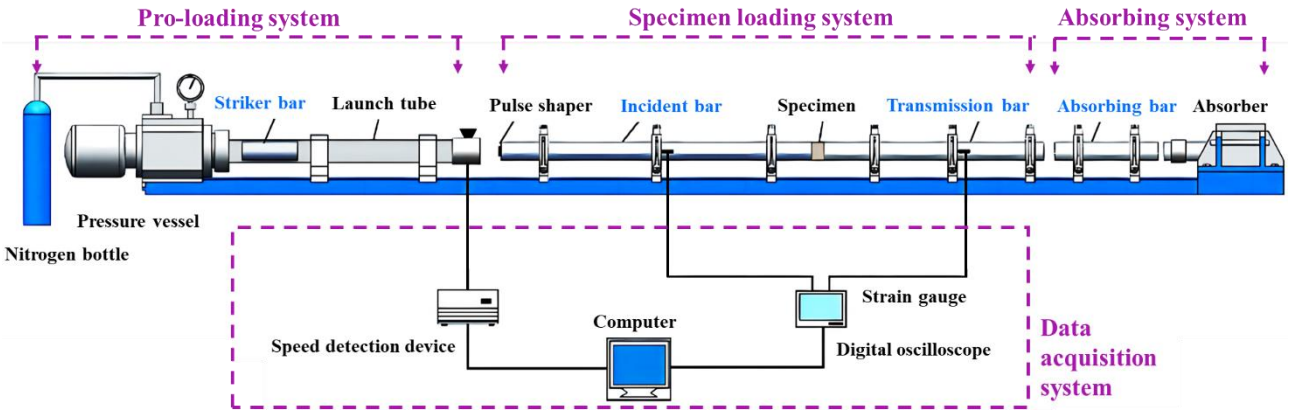

Fig. 3. Schematic illustration of SHPB device for the dynamic compressive test.

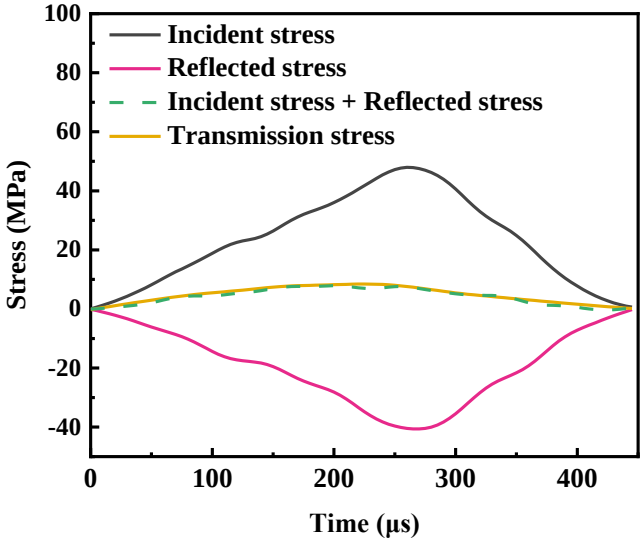

Fig. 4. An example of the stress equilibrium during the SHPB test.

2.5.4 Scanning electron microscopy

To characterise the microstructural evolution of ECC at elevated temperatures, SEM imaging (FEI, QUANTA FEG 250, USA) was conducted. Furthermore, a digital microscope was used to detect the fibre-matrix interface and morphology of some fracture pieces of the failed specimens after SHPB test with magnification ranges of 10–300.

2.5.5 Mercury intrusion porosimetry

The pore structural evolution of ECC was characterised using MIP (Mack Corporation, AutoPore IV 9500, USA). The test sample with a volume of less than 500 mm^3 and the pore size within the range of 0.001–1000 μm was measured.

3. Results and discussion

3.1 Ultrasonic pulse velocity

Fig. 5 depicts the propagation speed of ultrasonic in ECC at different temperatures. The UPV values

of ECC specimens increased first and reached the maximum at 105 °C, which was about 1.5% higher than that at 20 °C. This can be ascribed to the denser microstructure of ECC matrix and the bridging effect of PVA fibres that inhibited the crack growth [52]. Then, the UPV values dropped with the increase of elevated temperatures. Compared to that at 20 °C, the UPV values were reduced by 1.1%, 11.4%, 36.6% and 45.7% at 250, 400, 600 and 800 °C, respectively. At 250 °C, the presence of microcracks decreased the propagation velocity of the ultrasonic wave. When the temperature reached 400 °C, the vapour escaped through the pores formed by the melted fibres, mitigating the formation of microcracks [20]. However, as the porosity increased, the transmission distance of the ultrasonic wave was prolonged and the sound speed was thus reduced. A sharp reduction in ultrasonic wave velocity can be observed when the temperature went up from 400 to 800 °C. It can be mainly attributed to the formation of microcracks and the significant rise in porosity of the ECC matrix. Additionally, the reflection and detour phenomena would take place during the transmission process of ultrasonic waves which led to the increased travelling distance of ultrasonic wave in the specimens and the reduction of UPV values [53].

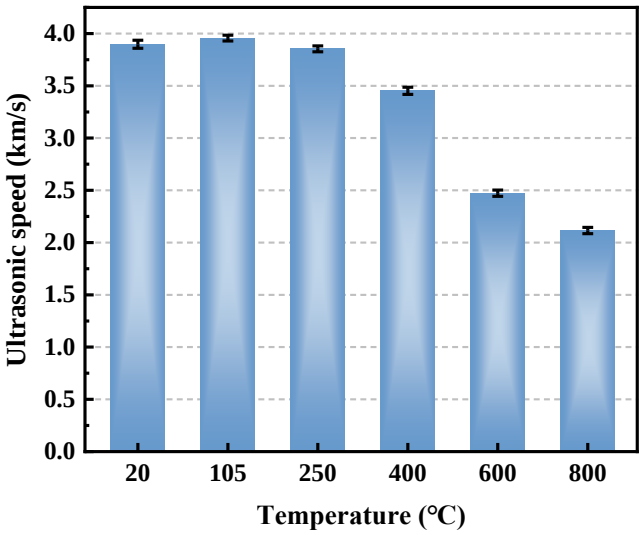

Fig. 5. Ultrasonic speed of ECC at elevated temperatures.

3.2 Quasi-static compressive strength

Fig. 6 demonstrates the quasi-static compressive strength of ECC specimens at elevated temperatures. The compressive strength of ECC specimens at 20 °C was 57.1 MPa, which was increased by 8.6% after exposure to 105 °C, respectively. It can be ascribed to the inclusion of fly ash in the ECC mixture and the induced high-temperature curing condition inside ECC that promoted the hydration of fly ash, resulting in a compact microstructure of the test block [54,55]. After that, a slight drop in compressive strength (about 14.0% lower than that at 20 °C) was found when the temperature reached 250 °C,

which can be ascribed to the melting of PVA fibres as well as microcracks induced by accumulated pore pressure. There exhibited a gradual reduction in compressive strength of ECC with the further rising temperature to 800 °C. At 400 °C, the compressive strength dropped by 11.0% compared to room temperature, while the difference was less than that of 250 °C, consistent with that presented in Ref. [19,56]. It is worth noting that approximately 75 wt% PVA fibres vaporised at 400 °C and the increased porosity within the concrete matrix led to a reduction in strength [21]. Compared to that at 20 °C, the compressive strength of ECC reduced by 34.3% at 600 °C and 70.6% at 800 °C, respectively. The continuous drop in compressive strength of ECC within this temperature range can be mainly explained by the decomposition of chemical composition and the increased number of pores and cracks inside matrix [57]. Additionally, the thermal stress can be generated within matrix due to the large temperature gradient before reaching the thermal equilibrium [58], which caused damage to the internal structure of ECC and also resulted in a reduction in compressive strength to a certain extent.

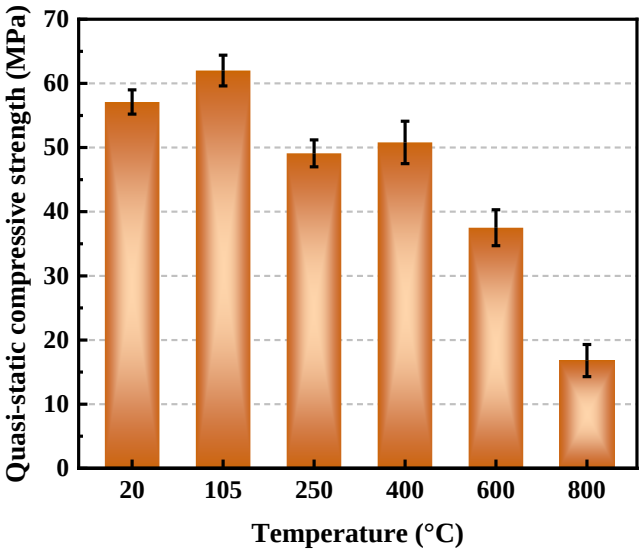

Fig. 6. 28 d compressive strength of ECC at elevated temperatures.

3.3 Dynamic compressive behaviour

3.3.1 Failure pattern

Fig. 7 displays the failure pattern of ECC specimens exposed to different temperatures under dynamic compression. The damage level of ECC increased with the rising strain rate and there exhibited various failure modes simultaneously with the increasing temperature. When the strain rate was around 79.8−81.2 s^{-1}, the specimens could maintain excellent integrity to a certain degree. Meanwhile, ECC showed obvious core retention failure mode under dynamic compressive load at 600 °C, with the number of fragments increased in large quantities. Within the strain rate range of 94.5−96.1 s^{-1},

the failure degree of ECC developed from peripheral crushing to crack propagation. Although the superficial cracks of specimens at 20 and 105 °C extended to the central area, the specimens can also be considered monolith under the effect of PVA fibre bridging. However, when the temperature reached 250 °C, the thermal decomposition of PVA fibre led to the loss of fibre bridging effect for ECC and the crushing scale of the specimen increased gradually. When the strain rate went up to 108.9−112.3 s^{-1}, the crack propagation zone on the surface or inside the matrix enlarged, along with the pull-out of PVA fibres under the rapid load. At this time, the fragment's number increased and the size changed from mesoscale to microscale compared to the relative strain rate of 94.5−96.1 s^{-1}. At a higher strain rate (123.5−127.1 s^{-1}), ECC specimens were destroyed completely due to the short time of crack growth in the specimen and the specimens were squeezed into fragments.

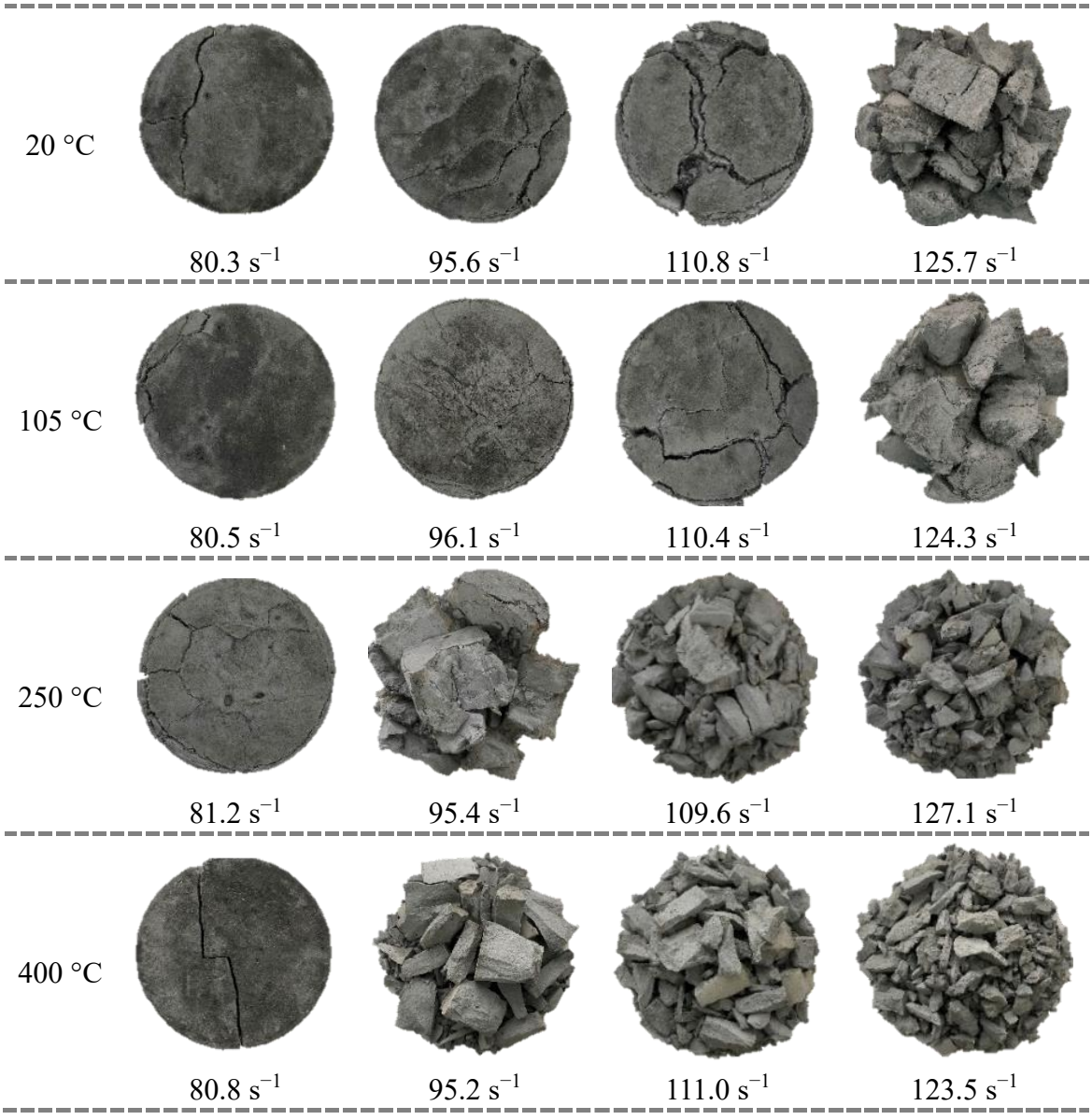

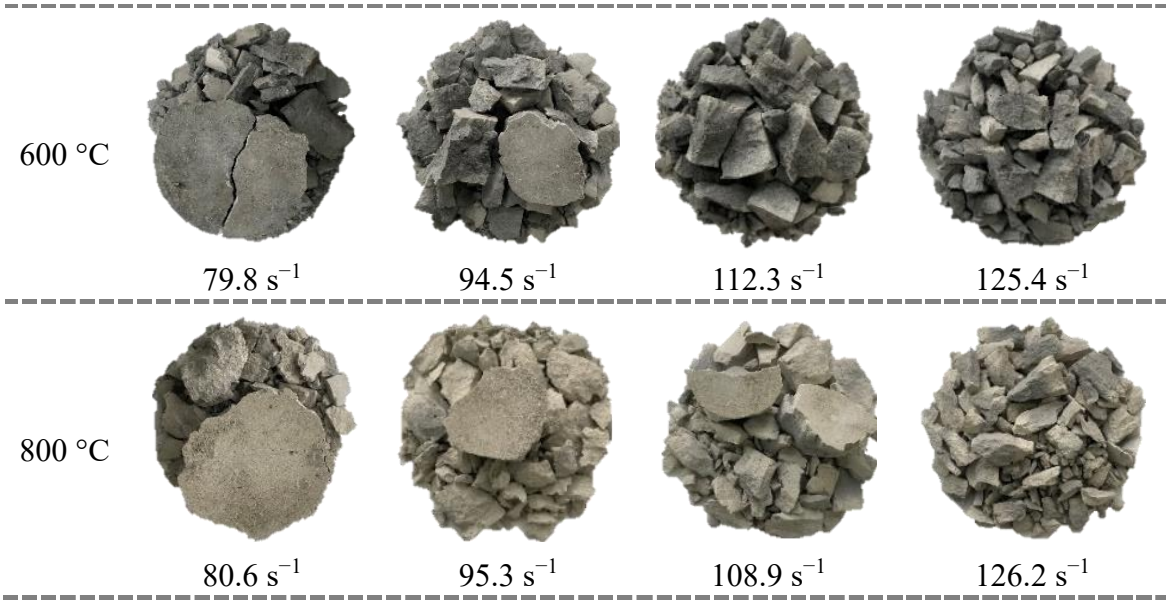

Fig. 7. Failure patterns of ECC specimens under dynamic compressive load.

Before fibre melting, the fibre-matrix bonding capability was effective and only partial crushing failure happened around the edge of the tested specimen. Moreover, the crack had enough time to propagate from the edge to the central area along the weak zone and disperse the impact energy [59]. With the rising strain rate, most PVA fibres were either pulled-out or broken, while the fibre-bridging effect still absorbed a certain amount of energy [39,41]. Above 250 °C, the outer parts of the specimen dropped under the impact load, resulting in the decline of fragment lumpiness with the increase of temperature. After the melting of PVA fibre, the failure condition became more serious than that at 20 °C and the impact resistance of ECC reduced. Hence, the elevated temperature aggravated the dynamic failure pattern of specimens which can be attributed to the thermal damage formed in matrix [60], and the dynamic compressive failure mode indicated obvious temperature sensitivity.

3.3.2 Stress-strain response

Fig. 8 presents the compressive stress-strain curves of ECC specimens exposed to elevated temperatures at strain rates of 79.8−127.1 s^{-1}. Overall, the stress-strain curves of ECC showed the same trend at various temperatures, where the peak stress went up while the maximum strain dropped with the increasing strain rate. Based on the changing trend of stress-strain curve, it can be classified as the pre-peak and post-peak stages. At the pre-peak stage, the stress increased linearly with the increase of strain and the slopes of curves decreased with the increase of strain rate. When the stress reached the peak value, the crack developed and the stress dropped with the rising strain due to the microcrack generation and propagation. PVA fibres were constantly pulled-out during the cracking process and thus the ultimate strain went up. With the rising strain rate, the compaction sustained time

of ECC under impact load was constantly shortened. During the post-peak stage, the stress of ECC specimen decreased until final failure due to the rapid growth of initial crack. At the same time, most of the PVA fibres experienced a slippage behaviour before they were completely pulled-out or ruptured, which agreed with the findings by other studies [33,61]. The impact deformation of ECC was controlled by fibre-matrix bond and the bridging effect of PVA fibre effectively improved the strain capacity and dynamic behaviour. When the temperature exceeded the melting point of PVA fibre, the impact resistance of ECC was mainly dependent on the strength of matrix.

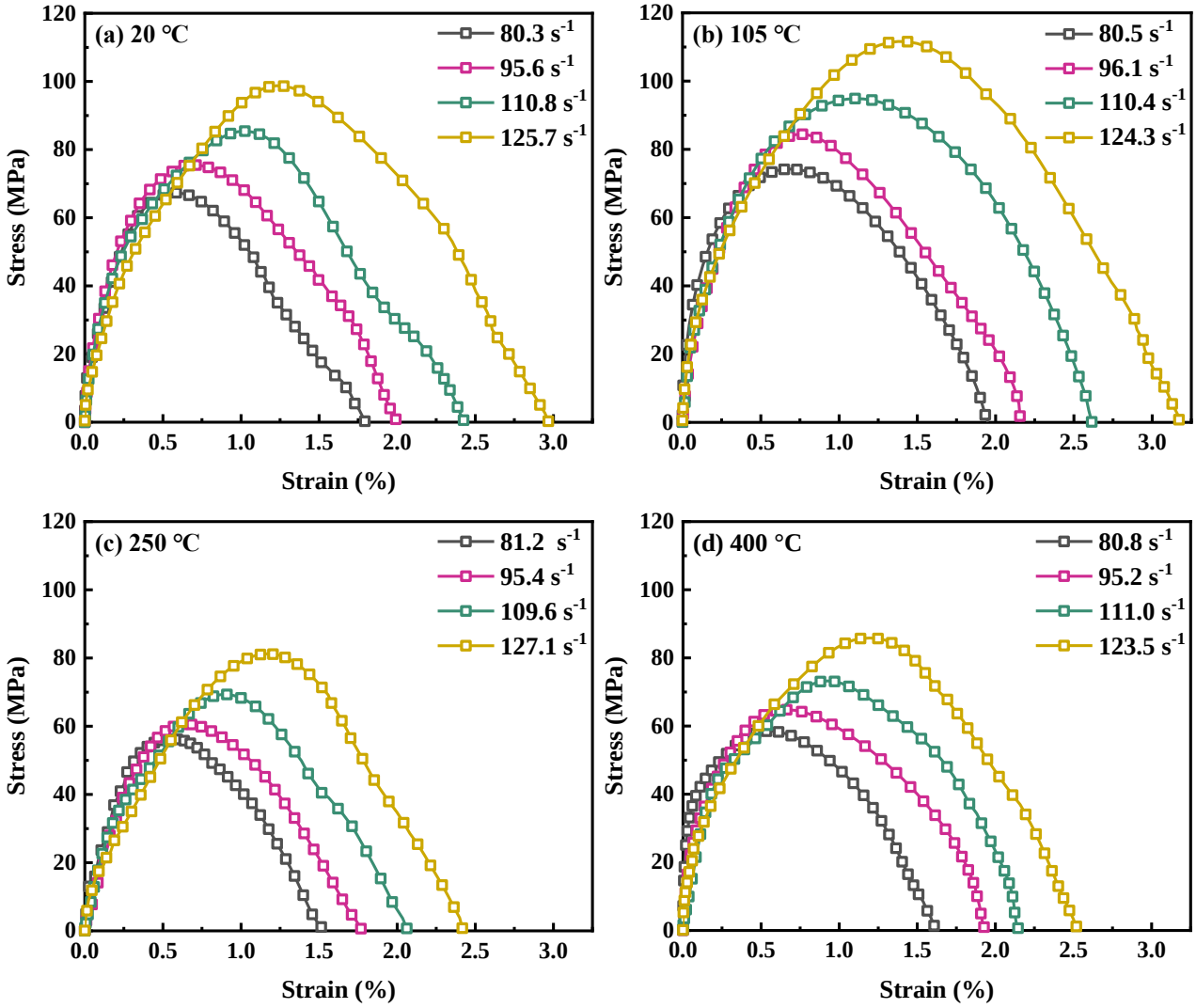

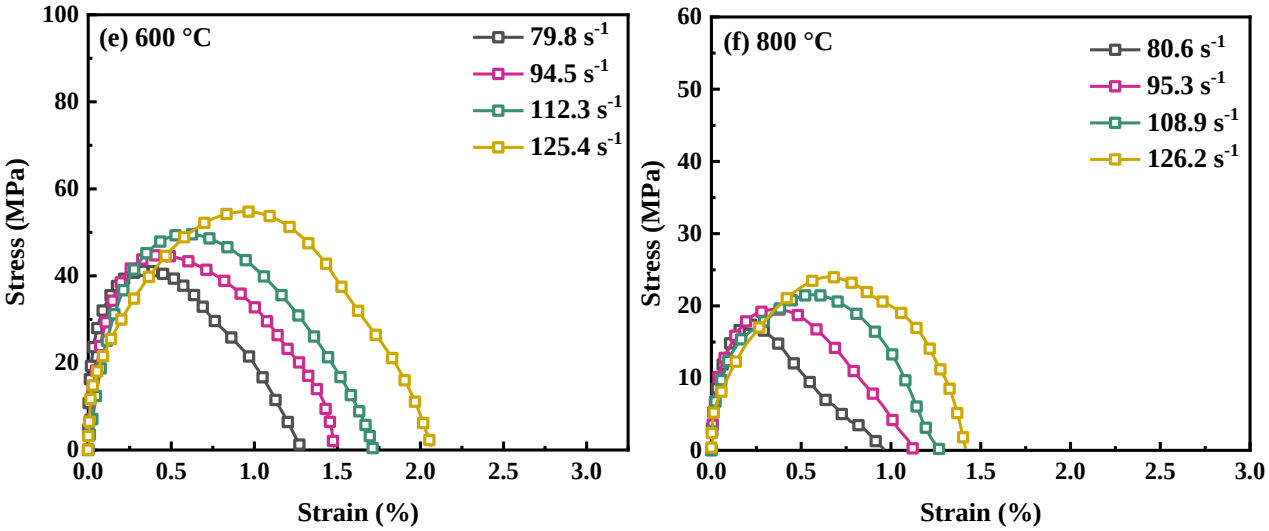

Fig. 8. Dynamic compressive stress-strain curves of ECC at elevated temperatures.

The dynamic strain capacity of ECC reflects its resistance to dynamic compressive load. It can be found that the strain at peak stress and the ultimate strain of ECC at various temperatures enlarged with the strain rate, indicating that high strain rates had an enhancing effect on the toughness of cementitious materials [62,63]. At the lower strain rate, the dynamic load improved the compaction degree of the matrix and expanded the strain-softening zone where ECC was damaged. With the rising strain rate, the compaction process was shortened and the ratio of peak strain to ultimate strain increased. The ultimate strain of ECC specimens at 20, 105, 250, 400, 600 and 800 °C was 2.37−3.07, 2.30−2.83, 2.08−2.70, 2.11−2.90, 2.14−3.69 and 2.16−4.36 times of the peak strain, respectively. Before 250 °C, the bridging effect of PVA fibres significantly increased the peak strain and ultimate strain of the specimens under dynamic compressive load, whilst enhancing the impact toughness and deformation resistance of ECC. As the exposure temperature went up, the microstructure of ECC became relatively unstable, leading to an obvious decline of strain capacity at 250−800 °C.

Fig. 9 displays the compressive stress-strain curves of ECC at a strain rate of 123.5−127.1 s^{-1}. The rising branch's slope of stress-strain curve at various temperatures increases with the peak stress, as well as the strain capacity of ECC. At 105 °C, the peak stress/strain and ultimate strain of the specimen reached the maximum. The interaction between PVA fibre and matrix effectively delayed the crack propagation under dynamic compressive load and improved the deformation resistance of ECC. With the melting of PVA fibre and the thermal damage of matrix, the stress and strain capacity of ECC reduced significantly [64]. Thus, the stress and strain of ECC were directly proportional to each other, regardless of elevated temperature.

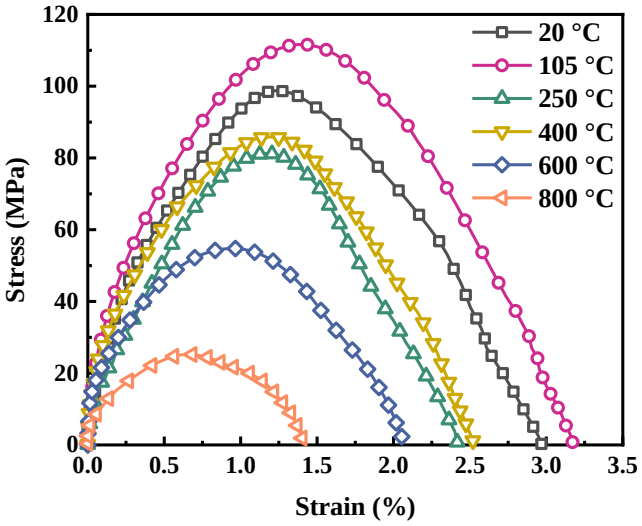

Fig. 9. Dynamic compressive stress-strain curves of ECC exposed to elevated temperatures at a strain rate of 123.5−127.1 s^{-1}.

3.3.3 Dynamic compressive strength

Fig. 10 illustrates the dynamic compressive strength of ECC at various exposure temperatures and strain rates, indicating the obvious strain rate effect of dynamic compressive strength of ECC at various temperatures. As strain rate increases, the mechanical response of specimens transfers from a one-dimensional stress state to a one-dimensional strain state, leading to an enhancement in strength [49]. Meanwhile, the energy required for crack generation of matrix is much higher than crack propagation and thus the rapid increase in the number of microcracks and internal stress enhances the resistance to impact load [65]. At 105 °C, the dynamic compressive strength of ECC went up by 10.2−13.0% compared to that at 20 °C, while the dynamic compressive strength of ECC at 250, 400, 600 and 800 °C dropped by 16.6−19.7%, 13.1−14.3%, 38.9−44.6% and 74.2−85.7% respectively against that at 20 °C. More PVA fibres around cracks played a strong bridging role under the impact load. Thus, ECC specimens had excellent dynamic compressive strength at 20 and 105 °C. Above 250 °C, the dynamic compressive strength of ECC dropped, but kept the similar level at 400 °C. For temperatures ranging from 600 to 800 °C, the growth rate of dynamic compressive strength of ECC declined significantly with the increase of strain rate. Overall, the microstructure of the matrix was seriously damaged with the increasing temperature and the dynamic compressive strength of ECC reduced greatly in consistence with normal concrete [66].

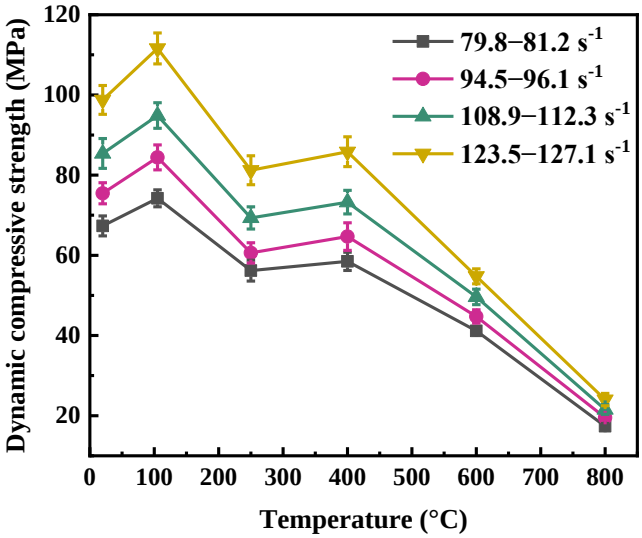

Fig. 10. Dynamic compressive strength of ECC at elevated temperatures.

3.3.4 Dynamic increase factor

As a parameter to quantitatively analyse the dynamic strength enhancement of materials, DIF is widely used to investigate the dynamic characteristics [32,67]. With the same load-bearing area, the DIF value of ECC specimen is obtained as the ratio of dynamic strength and quasi-static strength. Fig. 11a shows the evolution of compressive DIF under various strain rates with exposure temperature, indicating the same change trend as that of dynamic compressive strength. DIF of ECC exposed to various temperatures was greater than 1, suggesting the strain rate had a critical effect on the dynamic compressive strength of ECC. After exposure to 105 °C, DIF of ECC at different strain rates was 1.02−1.04 times that at 20 °C and at 250, 400, 600 and 800 °C, it was 93.2−96.6%, 96.0−97.7%, 84.4−93.2% and 82.3−88.1% of that at 20 °C, respectively. Before melting of PVA fibre, the effective bonding between PVA fibre and matrix under dynamic compressive load significantly improved the sensitivity of ECC to strain rate. After melting of PVA fibre, the microstructure of ECC was damaged at high temperatures and DIF dropped sharply with the rising temperature. Meanwhile, ECC was destroyed rapidly under higher strain rate. At higher temperature (over 600 °C), the microstructure of ECC matrix was seriously damaged after high temperature exposure and the strengthening effect of strain rate on DIF continued to weaken.

Different fitting methods have been adopted to elaborate the relationships between DIF and strain rate [41,49]. In this study, the fitted linear curve and curve equation between DIF and logarithm of strain rate for ECC at different temperatures are depicted in Fig. 11b. There is an obvious linear change trend between DIF and logarithm of strain rate. DIF of ECC at different temperatures showed a linear growth trend with the increase of logarithm of strain rate. The correlation coefficient (R^2) is greater than 0.9, indicating that the fitted equation had a high reliability and quality. The slopes of

fitted curves at 600 °C and 800 °C reduced significantly which confirmed that the strain rate enhancement effect of ECC dynamic properties was diminished at elevated temperature.

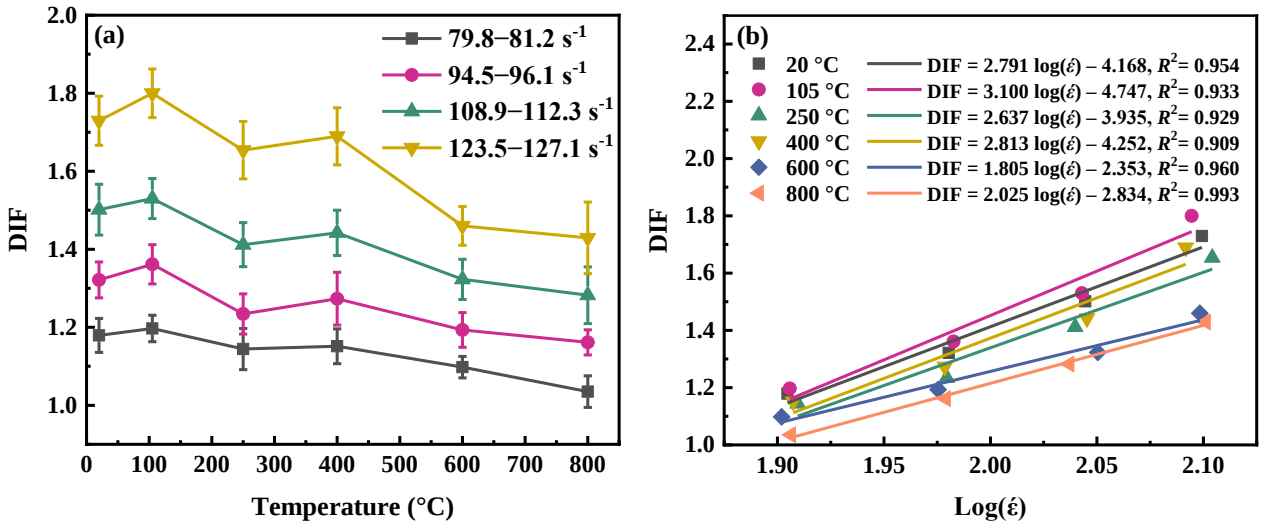

Fig. 11. (a) DIF of ECC at elevated temperatures; (b) Relationships between DIF and strain rate of ECC at elevated temperatures

Fig. 12 compares the DIF results of this study on ECC exposed to high temperatures and other studies on ECC [39,41], as well as the existing models including FIB model code [68] and CEB-FIP model code [69] for normal cementitious concrete with a transition strain rate of 30 s^{-1}. It also includes the DIF prediction model for ultra-high performance fibre reinforced concrete (UHPFRC) with a transition strain rate of 90 s^{-1}[70]. The equations are presented as follows:

$$\mathrm{DIF_{FIB}} = \begin{cases} \left(\dfrac{\dot{\varepsilon}}{\dot{\varepsilon}_1}\right)^{0.014}, & \dot{\varepsilon} \le 30\ s^{-1} \\ 0.012\left(\dfrac{\dot{\varepsilon}}{\dot{\varepsilon}_1}\right)^{1/3}, & \dot{\varepsilon} > 30\ s^{-1} \end{cases} \tag{2}$$

$$\mathrm{DIF_{CEB\text{-}FIP}} = \begin{cases} \left(\dfrac{\dot{\varepsilon}}{\dot{\varepsilon}_1}\right)^{1.026\alpha}, & \dot{\varepsilon} \le 30\ s^{-1} \\ \gamma\left(\dfrac{\dot{\varepsilon}}{\dot{\varepsilon}_1}\right)^{1/3}, & \dot{\varepsilon} > 30\ s^{-1} \end{cases} \tag{3}$$

$$\mathrm{DIF_{UHPFRC}} = \begin{cases} 0.0045\log(\dot{\varepsilon}) + 1.0206, & \dot{\varepsilon} < 90\ s^{-1} \\ 0.5874\log(\dot{\varepsilon}) - 0.1327, & \dot{\varepsilon} \ge 90\ s^{-1} \end{cases} \tag{4}$$

where $\dot{\varepsilon}_1$ is 0.00003 s^{-1}, α is $\left(5+9\frac{f_c}{f_{c1}}\right)^{-1}$, f_c represents the quasi-static compressive strength of the tested specimen, f_{c1} is 10 MPa, and γ is $10^{(6.156\alpha-2)}$.

As seen in Fig. 12, the results for ECC obtained from this study are in the middle region of normal concrete and UHPFRC, while the existing models cannot effectively predict the DIF of ECC. In addition, the test data of other studies show the similar change trends as this study. Thus, an increase

factor model for dynamic compression of ECC (2.0 vol% PVA fibre) using all the scatter data of Fig. 12 can be described as:

$$DIF_{ECC} = \begin{cases} 0.0218\log(\dot{\varepsilon}) + 1.0891, \dot{\varepsilon} \le 80\ s^{-1} \\ 1.8214\log(\dot{\varepsilon}) - 2.3120, \dot{\varepsilon} > 80\ s^{-1} \end{cases} \quad (5)$$

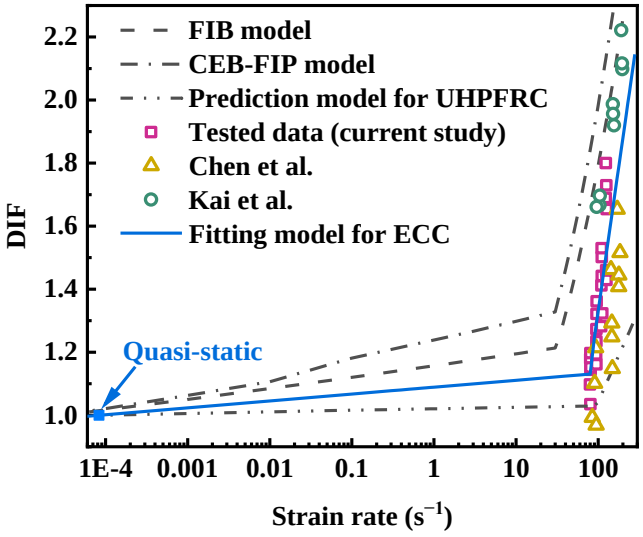

Fig. 12. DIF data and models obtained from the current study and literature [39,41,68–70].

3.3.5 Energy absorption capacity

Based on the relationship of the area under stress-stain curves and the volume of tested specimens, the energy absorption capacity of ECC before reaching the peak stress and during the whole failure process in the SHPB test is defined as fracture energy and dissipated energy, respectively. As seen in Fig. 13. The fracture energy and dissipated energy of ECC mostly improved with the strain rate under various high temperatures due to the formation of a greater number of microcracks [63]. The fracture energy and dissipated energy reached the maximum at 105 °C, which increased by 20.0−40.9% and 18.0−34.3%, relative to that of 20 °C, respectively. It can be explained by the improved bond between fibre and matrix at 105 °C [21,71]. At this time, the fibres at the crack were pulled out before reaching the peak stress. Because the absorption energy required for fibre pull-out was much greater than the energy required for fibre rupture, the fracture energy and dissipated energy of ECC were increased [72]. At 250, 400, 600 and 800 °C, the fracture energy and dissipated energy of ECC were 67.3−79.8%, 75.9−96.5%, 34.2−48.7% and 10.2−14.8%, as well as 67.9−73.4%, 80.0−88.5%, 43.8−47.3% and 12.4−14.7% of 20 °C, respectively. Above 250 °C, the rapid growth of a large number of microcracks and the extension of interfacial transition zone in the matrix reduced the energy dissipation of ECC, as a result of which the fracture energy and dissipation energy dropped rapidly. It is worth noting that the pores formed by the melting of PVA fibres in matrix played a certain role in energy absorption at

400 °C, resulting in a small rise in fracture energy and dissipation energy. When the temperature exceeded 600 °C, the decomposition of C−S−H gels, $CaCO_3$ and other components reduced the compactness and cohesion and microcrack initiated stress of matrix led to the rapid failure of ECC [25,73].

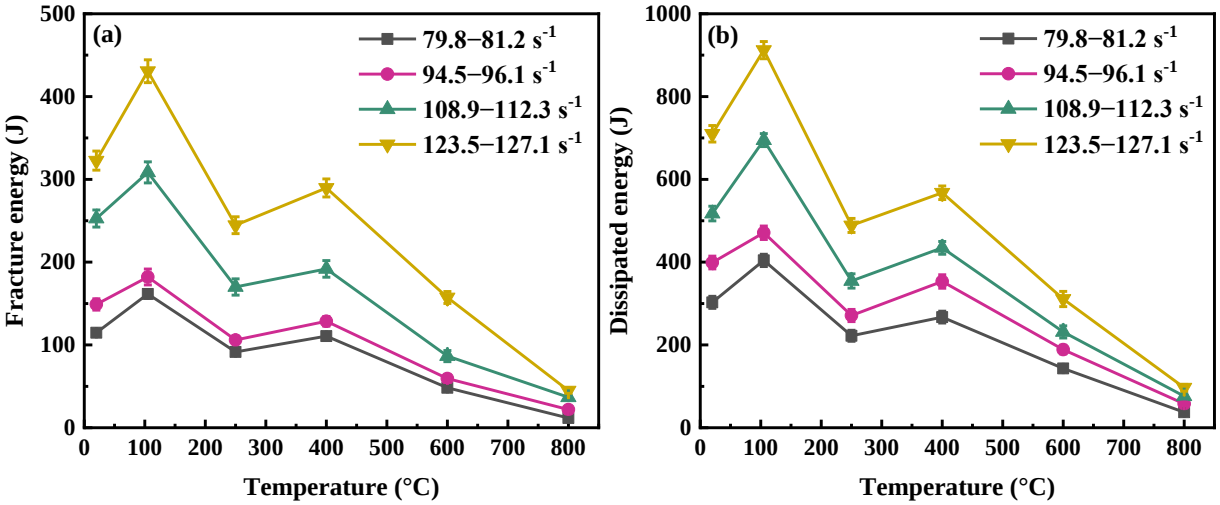

Fig. 13. Energy absorption of ECC at elevated temperatures: (a) fracture energy; (b) dissipated energy.

3.4 Microstructural evolution

3.4.1 Morphological evolution

Fig. 14 shows the SEM images of ECC after high-temperature exposure. PVA fibres inside ECC are effectively bonded to the matrix, as evidenced by the matrix fragments attached to the fibre surface (Fig. 14a). After exposure to 105 °C, there is an increase in the hydration gels on the surface of the matrix, along with the formation of cracks to the fibres from the internal surface of ECC (Fig. 14b), which enhanced the dynamic compressive properties of ECC at 105°C. Around the melting point (248 °C) and vaporization point (439 °C) of PVA fibres, the pores and needle-shaped channels appeared in the matrix surface (Fig. 14c and d). Due to the melting of PVA fibres, the impact resistance of ECC declined but the relatively lower matrix damage did not lead to the worst performance. Following this, the micro-cracks developed on the interface of matrix, which were generated on the walls of holes at 600 °C due to the decomposition of components and the effect of thermal stress (Fig. 14e). As seen in Fig. 14f, at 800 °C, the cracks extended along the aggregate as well as the interface of aggregate and cement paste, leading to the increased inhomogeneity [74]. Therefore, the combined effect of the melting of PVA fibres and the rapid matrix deterioration above 400 °C led to the most severe damage of ECC under impact load.

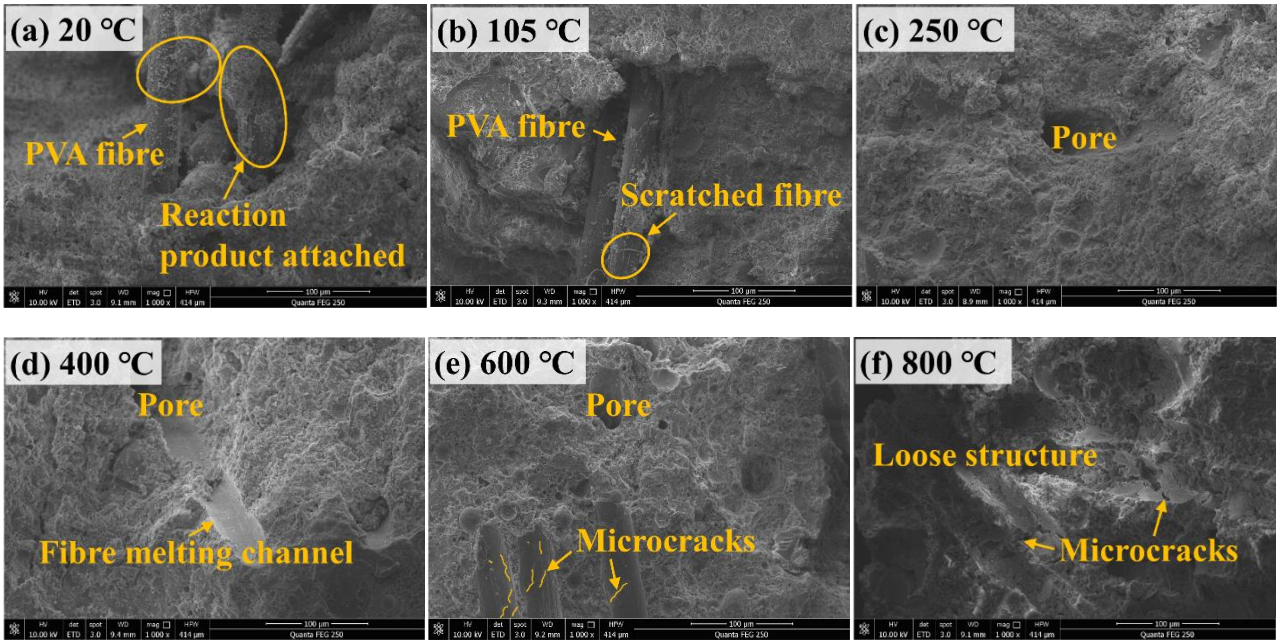

Fig. 14. SEM images of ECC at elevated temperatures.

The specimen resisted the impact load by increasing the internal stress and the generation of new cracks. With the increase of strain rate, the rapid growth of crack network absorbed the energy and the energy dissipation effect of ECC specimen was enhanced [30,33]. With the development of cracks, PVA fibres were constantly stretched to pull-out or rupture, while the fibre damage consumed a large amount of impact energy. Fig. 15 presents microscopic images of ECC at elevated temperatures under SHPB test. At 105 °C, the quasi-static mechanical strength of ECC went up due to higher compactness than ambient temperature, while the bond between PVA fibre and matrix developed. Under dynamic compressive load, the dissipated energy caused by slippage of PVA fibre increased and the destruction of more fibres is another reason for the improvement of dynamic performance of ECC (Fig. 15a and b). This resulted in the increase in dynamic compressive properties. Meanwhile, the energy consumed by crack initiation and propagation in matrix enlarged. When the temperature reached 250 °C (about the melting point of PVA fibre), the colour of PVA fibre on the surface of the specimen after heating turned brownish yellow (Fig. 15c). The melting condition of PVA fibre in matrix declined the impact resistance. Around 400 °C, needle channels and holes formed after evaporation of PVA fibres can be observed on the surface of the specimen (Fig. 15d). With the increasing number of pores in ECC matrix, the close of micro-pores brought a certain energy absorption effect and slightly improved the dynamic compressive properties of ECC [75]. During the temperature range of 400−800 °C, the hydration products of ECC began to decompose in large quantities and the aggregate was gradually separated from the cement matrix, resulting in the looser microstructure (Fig. 14) [76–78]. The dynamic loading accelerated the rate of crack/interface expansion due to the thermal effect which

caused severe strength loss in ECC. Then, the stress wave in the specimen cannot be transferred from the incident bar to the transmitted bar causing a reduction in absorbed energy which led to damage to the specimen under a less energetic dynamic load [66]. The energy dissipation of crack growth dropped with the rising temperature. Hence, the dynamic compressive properties of ECC can be adversely affected by elevated temperatures.

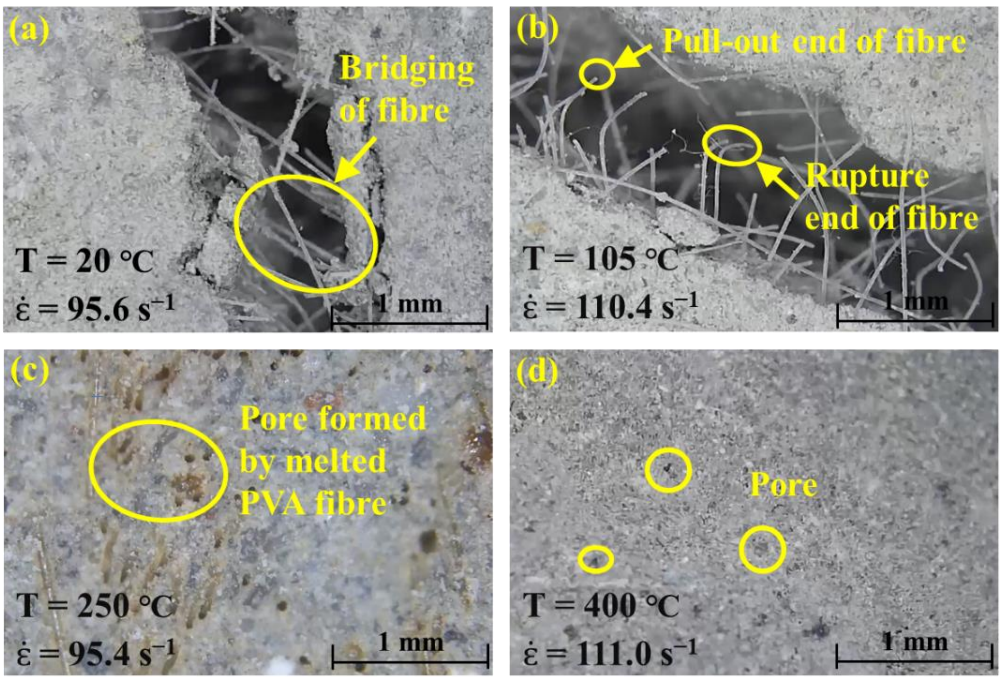

Fig. 15. Microscopic images of ECC under dynamic compressive test.

3.4.2 Pore structure evolution

After high-temperature exposure, the pore structure of ECC gradually changed, as indicated in the MIP test results. To evaluate the microstructure of ECC, pores of ECC can be divided into four types: macro (>2000 nm), transition (100−2000 nm), capillary (10−100 nm) and micro (<10 nm) pores [79,80]. Based on the theory of MIP measurement, the intruded work w_n and smallest pore radius r_n follow the relationship below [81].

$$\ln\left(\frac{w_n}{r_n^2}\right) = D_s \cdot \ln\left(\frac{v_n^{1/3}}{r_n}\right) + C \tag{6}$$

where v_n denotes the intruded mercury volume, D_s stands for the fractal dimension, and C is a constant.

Fig. 16 presents the logarithmic analysis of fractal dimensions of ECC and D_s for different regions. The pore structure of ECC showed typical fractal characteristics and D_s of macro/micro-factual regions were around 2−3 with cylindrical pores. Partial D_s of transition/capillary zone was beyond 3 due to the existence of uniform pores (e.g., ink-bottle pores) in the pore range of 25−100 nm, which lost its initial significance [82,83]. In addition, D_s beyond 2−3 was excluded to ensure the accuracy

of calculations of the remaining fractal regions [80]. Hence, the focus was placed on the macro/micro-factual regions. Generally, D_s of macro-factual at elevated temperatures had less variation except for a sudden rise at 800 °C, which can be ascribed to the severe damage of microstructure. However, D_s of micro-factual showed a trend of first rise up to 250 °C and then drop until 800 °C due to the pozzolanic reaction of unhydrated cement or fly ash particles before 250 °C [10,15,16,73]. After 250 °C, the microscopic composition decomposed considerably causing a rapid decline in the volume and strength of the gels up to 800 °C [18,24,25].

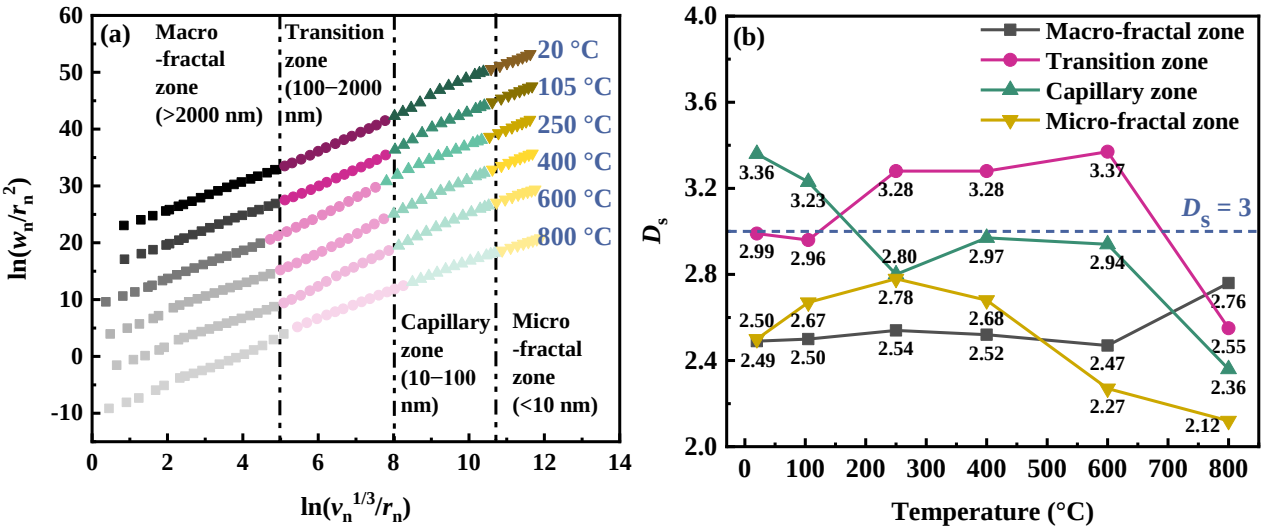

Fig. 16. Fractal analysis of ECC at elevated temperature: (a) logarithm plots of $\ln(w_n/r_n^2)$ and $\ln(v_n^{1/3}/r_n)$; (b) D_s in various pore ranges.

The evolution of pore structure is an important factor affecting the mechanical properties of cementitious materials after exposure to high temperatures. Most studies on dynamic mechanical properties have been focused on the strain rate enhancement of the material or the change with exposure temperature, while the relationship between its microstructure and dynamic compressive parameters has not been well explored. Based on the above test results of dynamic compressive properties of ECC (Section 3.3) and the fractal analysis of pore structure, the relationship between microstructure and dynamic compressive properties of ECC at elevated temperatures is established, as shown in Fig. 17. The dynamic compressive strength and energy absorption of ECC's macro/micro-fractal zone increased and then reduced with the increasing D_s, indicating a parabolic relation with the maximum value at 105 °C as opposed to linear trend of previous studies [84,85]. Compared to the relatively scattered D_s of micro-fractal zone (Fig. 17b and d), the most D_s of macro-fractal zone mainly concentrated around 2.50 (Fig. 17a and c). The dynamic compressive strength and energy absorption of ECC under various strain rates and their strain rate effect dropped as the difference between D_s and 2.50 went up. Moreover, the change of energy absorption capacity with strain rate

was greater than that of strength for the same D_s. The more complicated pore structure, the larger D_s, as D_s can indicate the complexity of pore structure [86]. For the same complexity of pore structure, energy absorption had a more significant strain rate enhancement effect than dynamic compressive strength.

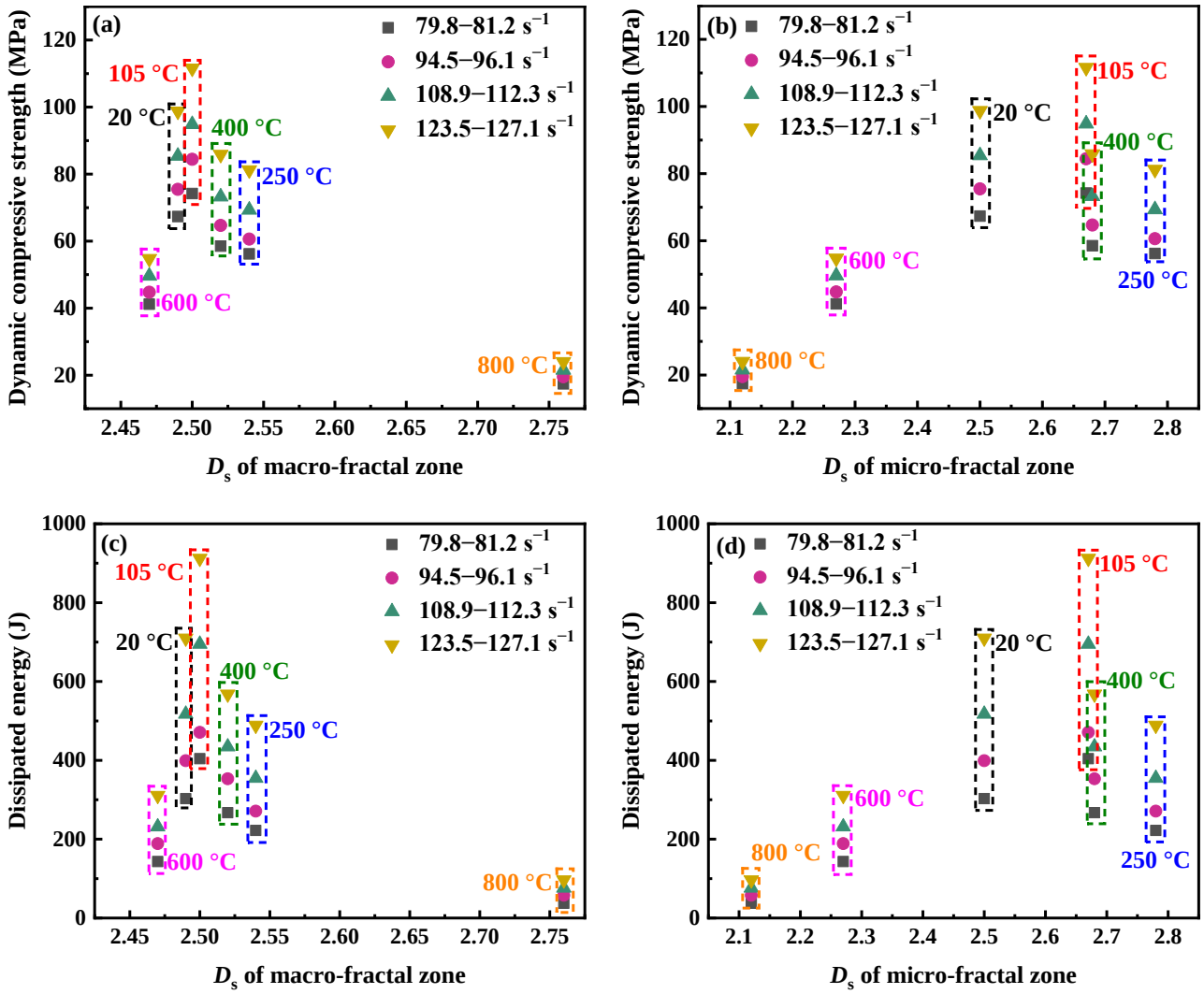

Fig. 17. Relationship between D_s in macro/micro fractal region and dynamic properties of ECC.

Under dynamic loading, the corners of irregularly shaped pores within cementitious composites were prone to suffer stress concentration, causing crack initiation. With the rising strain rates, the rate of crack growth within matrix accelerates and the pore structure exhibits strain rate sensitivity [84]. The dynamic properties of ECC were influenced by the fibre incorporation and the effect of fibre addition on the matrix, which changed differently at elevated temperatures. The micromechanics between the fibres and matrix of ECC led to the existence of an optimum state on strength as influenced by the pore structure, where D_s of the air (macro) and gel (micro) pores could be fully considered in the analysis. This resulted in the highest dynamic mechanical properties at a certain D_s value, which was at 105 °C. At this point, PVA fibres generated maximum slip from within the matrix

of a pore structure (D_s of the air and gel pores were 2.50 and 2.67, respectively), ensuring the most efficient dynamic load resistance and energy absorption capacity. In addition, the relationship between the transition/capillary fractal zone of pore structure and static/dynamic compressive behaviour at high temperatures and the proportion of the effect of different pore structures needs to be further explored.

4. Conclusions

In this study, the dynamic behaviour of ECC exposed to elevated temperatures was systematically investigated through a series of tests. Based on the obtained experimental results as well as fractal analysis, the main conclusions can be drawn as follows:

- PVA fibre played an effective bridging role in the dynamic compression process in ECC, which reduced the damage degree. With the increase of strain rate, the specimen broke into fragments gradually at 20 and 105 °C. After the melting of PVA fibre, the number of fragments increased and the scale decreased progressively, leading to an obvious brittle failure mode under dynamic compressive load.
- The dynamic compressive properties of ECC exposed to various temperatures increased with the rising strain rate. The dynamic compressive strength and dissipated energy of ECC at a strain rate of 123.5−127.1 s^{-1} went up by 33.0−50.4% and 112.4−150.3% respectively relative to that at 79.8−81.2 s^{-1}. DIF on dynamic compressive strength of ECC varied from 1.04 to 1.80 in the exposure temperature range of 20−800 °C. The established model gave favourable predictions of dynamic properties of ECC at various strain rates.
- The dynamic compressive properties of ECC reached the maximum at 105 °C and declined over 250 °C due to the melting of PVA fibres and the rising number of cracks in matrix, which worsened the dynamic compressive performance of ECC. At 800 °C, the dynamic compressive strength and dissipated energy of ECC dropped by 74.2−85.7% and 85.3−87.6% respectively compared to that at 20 °C due to the disintegration of components and deterioration of microstructure.
- The degradation degree of ECC under dynamic compressive load was higher than that under quasi-static compressive load due to the microcrack propagation and pore structural evolution. The appearance of large number of pores or microcracks in matrix and the decomposition of hydration products impaired the impact resistance of ECC. The fractal analysis of gel pores and air pores indicated that the pore structure of ECC at 105 °C was ideal for the highest mechanical properties, with fractal dimensions of 2.50 and 2.67, respectively.

The microstructural evolution and mechanical properties of ECC exposed to elevated temperatures were investigated in this study. To further improve the sustainability and high-temperature/fire resistance of ECC for wider engineering applications, the high-cost PVA fibres can be replaced by recycled fibres (e.g., recycled tyre polymer fibres) [87], and inorganic fibres with a higher melting point (e.g., steel fibres) can be incorporated [88], which is the subject of ongoing research and will be presented in future publications.

Acknowledgements

The authors gratefully acknowledge the financial support from the National Natural Science Foundation of China (No. 52178382), the Fundamental Research Funds for the Central Universities (No. N2201023), and the Doctoral Initial Research Funds of Liaoning Province.

References

[1] V.C. Li, Engineered Cementitious Composites (ECC) : Bendable Concrete for Sustainable and Resilient Infrastructure, Springer, 2019, Springer, 2019. https://doi.org/10.1007/978-3-662-58438-5.

[2] C.K.Y. Leung, Design criteria for pseudoductile fiber-reinforced composites, J. Eng. Mech. 122 (1996) 10–18. https://doi.org/10.1061/(ASCE)0733-9399(1996)122:1(10).

[3] M. Singh, B. Saini, H.D. Chalak, Performance and composition analysis of engineered cementitious composite (ECC) – A review, J. Build. Eng. 26 (2019) 100851. https://doi.org/10.1016/j.jobe.2019.100851.

[4] S. Wang, V.C. Li, Engineered cementitious composites with high-volume fly ash, ACI Mater. J. 104 (2007) 233–241. https://doi.org/10.14359/18668.

[5] V.C. Li, C. Wu, S.X. Wang, A. Ogawa, T. Saito, Interface tailoring for strain-hardening polyvinyl alcohol engineered cementitious composite (PVA-ECC), Aci Mater. J. 99 (2002) 463–472. https://doi.org/10.1016/S0042-207X(02)00187-2.

[6] V.C. Li, Tailoring ECC for special attributes: A review, Int. J. Concr. Struct. Mater. 6 (2012) 135–144. https://doi.org/10.1007/s40069-012-0018-8.

[7] V.C. Li, M. Lepech, L. Lepech, Crack Resistant Concrete Material for Transportation Construction, Transp. Res. Board 83rd Annu. Meet. Washington, DC, CD Rom 04-4680. (2003) 4–4680.

[8] Z. Chen, Y. Yang, Y. Yao, Impact properties of engineered cementitious composites with high volume fly ash using SHPB test, J. Wuhan Univ. Technol. Mater. Sci. Ed. 27 (2012)

590–596. https://doi.org/10.1007/s11595-012-0511-6.

[9] K.Q. Yu, L.Z. Li, J.T. Yu, Y.C. Wang, J.H. Ye, Q.F. Xu, Direct tensile properties of engineered cementitious composites: A review, Constr. Build. Mater. 165 (2018) 346–362. https://doi.org/10.1016/j.conbuildmat.2017.12.124.

[10] P.S. Bhat, V. Chang, M. Li, Effect of elevated temperature on strain-hardening engineered cementitious composites, Constr. Build. Mater. 69 (2014) 370–380. https://doi.org/10.1016/j.conbuildmat.2014.07.052.

[11] J.R. Zhang, T. Lv, Y. Zhu, D.S. Hou, Damage mechanism of engineered cementitious composites after exposed to elevated temperatures: Experimental and molecular dynamics study, Cem. Concr. Compos. 129 (2022) 104507. https://doi.org/10.1016/j.cemconcomp.2022.104507.

[12] A. Mohammedameen, M.E. Gülşan, R. Alzeebaree, A. Çevik, A. Niş, Mechanical and durability performance of FRP confined and unconfined strain hardening cementitious composites exposed to sulfate attack, Constr. Build. Mater. 207 (2019) 158–173. https://doi.org/10.1016/j.conbuildmat.2019.02.108.

[13] T. Wang, D. Zhang, H. Zhu, B. Ma, V.C. Li, Durability and self-healing of engineered cementitious composites exposed to simulated sewage environments, Cem. Concr. Compos. 129 (2022). https://doi.org/10.1016/j.cemconcomp.2022.104500.

[14] H. Liu, Q. Zhang, V. Li, H. Su, C. Gu, Durability study on engineered cementitious composites (ECC) under sulfate and chloride environment, Constr. Build. Mater. 133 (2017) 171–181. https://doi.org/10.1016/j.conbuildmat.2016.12.074.

[15] M. Sahmaran, E. Ozbay, H.E. Yucel, M. Lachemi, V.C. Li, Effect of Fly Ash and PVA Fiber on Microstructural Damage and Residual Properties of Engineered Cementitious Composites Exposed to High Temperatures, J. Mater. Civ. Eng. 23 (2011) 1735–1745. https://doi.org/10.1061/(asce)mt.1943-5533.0000335.

[16] Z.G. Zhang, J.C. Liu, X.Q. Xu, L.Q. Yuan, Effect of sub-elevated temperature on mechanical properties of ECC with different fly ash contents, Constr. Build. Mater. 262 (2020) 120096. https://doi.org/10.1016/j.conbuildmat.2020.120096.

[17] S. Sanchayan, S.J. Foster, High temperature behaviour of hybrid steel–PVA fibre reinforced reactive powder concrete, Mater. Struct. Constr. 49 (2016) 769–782. https://doi.org/10.1617/s11527-015-0537-2.

[18] K.Q. Yu, J.G. Dai, Z.D. Lu, C.K.Y. Leung, Mechanical properties of engineered cementitious composites subjected to elevated temperatures, J. Mater. Civ. Eng. 27 (2015) 4014268. https://doi.org/10.1061/(Asce)Mt.1943-5533.0001241.

[19] A.A. Deshpande, D. Kumar, R. Ranade, Influence of high temperatures on the residual mechanical properties of a hybrid fiber-reinforced strain-hardening cementitious composite, Constr. Build. Mater. 208 (2019) 283–295. https://doi.org/10.1016/j.conbuildmat.2019.02.129.

[20] M. Chen, Z.H. Sun, W.L. Tu, X. Yan, M.Z. Zhang, Behaviour of recycled tyre polymer fibre reinforced concrete at elevated temperatures, Cem. Concr. Compos. 124 (2021) 104257. https://doi.org/10.1016/j.cemconcomp.2021.104257.

[21] C.L. Chan, M. Zhang, Behaviour of strain hardening geopolymer composites at elevated temperatures, Cem. Concr. Compos. 132 (2022) 104634. https://doi.org/10.1016/j.cemconcomp.2022.104634.

[22] J.C. Liu, K.H. Tan, Mechanism of PVA fibers in mitigating explosive spalling of engineered cementitious composite at elevated temperature, Cem. Concr. Compos. 93 (2018) 235–245. https://doi.org/10.1016/j.cemconcomp.2018.07.015.

[23] M. Sahmaran, M. Lachemi, V.C. Li, Assessing Mechanical Properties and Microstructure of Fire-Damaged Engineered Cementitious Composites, Aci Mater. J. 107 (2010) 297–304. https://doi.org/10.14359/51663759.

[24] J.C. Liu, K.H. Tan, Fire resistance of strain hardening cementitious composite with hybrid PVA and steel fibers, Constr. Build. Mater. 135 (2017) 600–611. https://doi.org/10.1016/j.conbuildmat.2016.12.204.

[25] T.K. Erdem, Specimen size effect on the residual properties of engineered cementitious composites subjected to high temperatures, Cem. Concr. Compos. 45 (2014) 1–8. https://doi.org/10.1016/j.cemconcomp.2013.09.019.

[26] X.L. Li, Y. Bao, L.L. Wu, Q.X. Yan, H.Y. Ma, G.D. Chen, H.N. Zhang, Thermal and mechanical properties of high-performance fiberreinforced cementitious composites after exposure to high temperatures, Constr. Build. Mater. 157 (2017) 829–838. https://doi.org/10.1016/j.conbuildmat.2017.09.125.

[27] T. Zhang, M. Zhang, Y. Shen, H. Zhu, Z. Yan, Mitigating the damage of ultra-high performance concrete at elevated temperatures using synergistic flame-retardant polymer

fibres, Cem. Concr. Res. 158 (2022) 106835. https://doi.org/10.1016/J.CEMCONRES.2022.106835.

[28] Q. Wang, B.Y. Yao, R.Z. Lu, Behavior deterioration and microstructure change of polyvinyl alcohol fiber-reinforced cementitious composite (PVA-ECC) after exposure to elevated temperatures, Materials (Basel). 13 (2020) 5539. https://doi.org/10.3390/ma13235539.

[29] K.Q. Yu, Z.D. Lu, J.T. Yu, Residual compressive properties of strain-hardening cementitious composite with different curing ages exposed to high temperature, Constr. Build. Mater. 98 (2015) 146–155. https://doi.org/10.1016/j.conbuildmat.2015.08.041.

[30] Q. Yu, W. Zhuang, C. Shi, Research progress on the dynamic compressive properties of ultra-high performance concrete under high strain rates, Cem. Concr. Compos. 124 (2021) 104258. https://doi.org/10.1016/j.cemconcomp.2021.104258.

[31] H. Zhang, L. Wang, K. Zheng, T.J. Bakura, P.G. Totakhil, Research on compressive impact dynamic behavior and constitutive model of polypropylene fiber reinforced concrete, Constr. Build. Mater. 187 (2018) 584–595. https://doi.org/10.1016/j.conbuildmat.2018.07.164.

[32] Z. Wu, C. Shi, W. He, D. Wang, Static and dynamic compressive properties of ultra-high performance concrete (UHPC) with hybrid steel fiber reinforcements, Cem. Concr. Compos. 79 (2017) 148–157. https://doi.org/10.1016/j.cemconcomp.2017.02.010.

[33] H. Zhong, M. Zhang, Effect of recycled polymer fibre on dynamic compressive behaviour of engineered geopolymer composites, Ceram. Int. 48 (2022) 23713–23730. https://doi.org/10.1016/j.ceramint.2022.05.023.

[34] Q. Li, X. Zhao, S. Xu, X. Gao, Influence of steel fiber on dynamic compressive behavior of hybrid fiber ultra high toughness cementitious composites at different strain rates, Constr. Build. Mater. 125 (2016) 490–500. https://doi.org/10.1016/j.conbuildmat.2016.08.066.

[35] Y. Hao, H. Hao, G.P. Jiang, Y. Zhou, Experimental confirmation of some factors influencing dynamic concrete compressive strengths in high-speed impact tests, Cem. Concr. Res. 52 (2013) 63–70. https://doi.org/10.1016/j.cemconres.2013.05.008.

[36] P.H. Bischoff, S.H. Perry, Compressive behaviour of concrete at high strain rates, Mater. Struct. 24 (1991) 425–450. https://doi.org/10.1007/BF02472016.

[37] J. Lai, W. Sun, Dynamic behaviour and visco-elastic damage model of ultra-high performance cementitious composite, Cem. Concr. Res. 39 (2009) 1044–1051. https://doi.org/10.1016/j.cemconres.2009.07.012.

[38] M. Zhang, H.J. Wu, Q.M. Li, F.L. Huang, Further investigation on the dynamic compressive strength enhancement of concrete-like materials based on split Hopkinson pressure bar tests. Part I: Experiments, Int. J. Impact Eng. 36 (2009) 1327–1334. https://doi.org/10.1016/j.ijimpeng.2009.04.009.

[39] M.F. Kai, Y. Xiao, X.L. Shuai, G. Ye, Compressive Behavior of Engineered Cementitious Composites under High Strain-Rate Loading, J. Mater. Civ. Eng. 29 (2017) 1–8. https://doi.org/10.1061/(asce)mt.1943-5533.0001781.

[40] J.X. Lin, Y. Song, Z.H. Xie, Y.C. Guo, B. Yuan, J.J. Zeng, X. Wei, Static and dynamic mechanical behavior of engineered cementitious composites with PP and PVA fibers, J. Build. Eng. 29 (2020) 101097. https://doi.org/10.1016/j.jobe.2019.101097.

[41] Z. Chen, Y. Yang, Y. Yao, Quasi-static and dynamic compressive mechanical properties of engineered cementitious composite incorporating ground granulated blast furnace slag, Mater. Des. 44 (2013) 500–508. https://doi.org/10.1016/j.matdes.2012.08.037.

[42] Q. Li, X. Zhao, S. Xu, C.K.Y. Leung, B. Wang, Multiple Impact Resistance of Hybrid Fiber Ultrahigh Toughness Cementitious Composites with Different Degrees of Initial Damage, J. Mater. Civ. Eng. 31 (2019) 1–13. https://doi.org/10.1061/(asce)mt.1943-5533.0002576.

[43] GB/T 175-2007, Common Portland Cement, Chinese national standard, 2007.

[44] ASTM C618-17a, Standard Specification for Coal Fly Ash and Raw or Calcined Natural Pozzolan for Use in Concrete, ASTM International, West Conshohocken, PA, 2017, n.d.

[45] E.H. Yang, S. Wang, Y. Yang, V.C. Li, Fiber-bridging constitutive law of engineered cementitious composites, J. Adv. Concr. Technol. 6 (2008) 181–193. https://doi.org/10.3151/jact.6.181.

[46] GB/T50081-2019, Standard for test methods of concrete physical and mechanical properties, China Building Materials Academy, China, 2019.

[47] ASTM E831-14, Standard Test Method for Linear Thermal Expansion of Solid Materials by Thermomechanical Analysis, ASTM International, West Conshohocken, PA, 2019.

[48] ASTM C469, Standard test method for static modulus of elasticity and Poisson's ratio of concrete in compression, ASTM International, West Conshohocken, PA, United States, 2014, n.d.

[49] M. Chen, W. Chen, H. Zhong, D. Chi, Y.H. Wang, M.Z. Zhang, Experimental study on dynamic compressive behaviour of recycled tyre polymer fibre reinforced concrete, Cem.

Concr. Compos. 98 (2019) 95–112. https://doi.org/10.1016/j.cemconcomp.2019.02.003.

[50] M. Chen, H. Si, X. Fan, Y. Xuan, M. Zhang, Dynamic compressive behaviour of recycled tyre steel fibre reinforced concrete, Constr. Build. Mater. 316 (2022) 125896. https://doi.org/10.1016/j.conbuildmat.2021.125896.

[51] W.W. Chen, B. Song, Split Hopkinson (Kolsky) Bar: Design, Testing and Applications, Springer, 2011.

[52] S. Abdi, R. Demirboga, W.H. Khushefati, Relationship between compressive strength and UPV of GGBFS based geopolymer mortars exposed to elevated temperatures, Constr. Build. Mater. 94 (2015) 189–195. https://doi.org/10.1016/j.conbuildmat.2015.07.006.

[53] M. Uysal, Self-compacting concrete incorporating filler additives : Performance at high temperatures, Constr. Build. Mater. 26 (2012) 701–706. https://doi.org/10.1016/j.conbuildmat.2011.06.077.

[54] J.C. Liu, K.H. Tan, D. Zhang, Multi-response optimization of post-fire performance of strain hardening cementitious composite, Cem. Concr. Compos. 80 (2017) 80–90. https://doi.org/10.1016/j.cemconcomp.2017.03.001.

[55] J.T. Yu, J.H. Lin, Z.G. Zhang, V.C. Li, Mechanical performance of ECC with high-volume fly ash after sub-elevated temperatures, Constr. Build. Mater. 99 (2015) 82–89. https://doi.org/10.1016/j.conbuildmat.2015.09.002.

[56] M. Chen, Y. Wang, T. Zhang, M. Zhang, Behaviour of structural engineered cementitious composites under dynamic tensile loading and elevated temperatures, Eng. Struct. 280 (2023) 115739. https://doi.org/10.1016/j.engstruct.2023.115739.

[57] T. Zhang, M. Chen, Z. Yan, S. Wang, M. Zhang, Role of micro fibres in tailoring the specific heat capacity of cementitious composites at elevated temperatures: Experimental characterisation and micromechanical modelling, Constr. Build. Mater. 369 (2023) 130550. https://doi.org/10.1016/J.CONBUILDMAT.2023.130550.

[58] D. Zhang, A. Dasari, K.H. Tan, On the mechanism of prevention of explosive spalling in ultra-high performance concrete with polymer fibers, Cem. Concr. Resea. 113 (2018) 169–177. https://doi.org/10.1016/j.cemconres.2018.08.012.

[59] Q. Fu, D. Niu, J. Zhang, D. Huang, M. Hong, Impact response of concrete reinforced with hybrid basalt-polypropylene fibers, Powder Technol. 326 (2018) 411–424. https://doi.org/10.1016/j.powtec.2017.12.022.

[60] X. Liang, C. Wu, Y. Yang, Z. Li, Experimental study on ultra-high performance concrete with high fire resistance under simultaneous effect of elevated temperature and impact loading, Cem. Concr. Compos. 98 (2019) 29–38. https://doi.org/10.1016/j.cemconcomp.2019.01.017.

[61] B. Zhang, Y. Feng, J. Xie, J. He, Y. Zhang, C. Cai, D. Huang, L. Li, Effects of fibres on ultra-lightweight high strength concrete: Dynamic behaviour and microstructures, Cem. Concr. Compos. 128 (2022) 104417. https://doi.org/10.1016/j.cemconcomp.2022.104417.

[62] Q.X. Le, J.L. Torero, V.T.N. Dao, Stress–strain–temperature relationship for concrete, Fire Saf. J. 120 (2021) 103126. https://doi.org/10.1016/j.firesaf.2020.103126.

[63] W. Ren, J. Xu, H. Su, Dynamic compressive behaviour of concrete after exposure to elevated temperatures, Mater. Struct. Constr. 49 (2016) 3321–3334. https://doi.org/10.1617/s11527-015-0722-3.

[64] Q. Ma, R. Guo, Z. Zhao, Z. Lin, K. He, Mechanical properties of concrete at high temperature-A review, Constr. Build. Mater. 93 (2015) 371–383. https://doi.org/10.1016/j.conbuildmat.2015.05.131.

[65] Q.M. Li, H. Meng, About the dynamic strength enhancement of concrete-like materials in a split Hopkinson pressure bar test, Int. J. Solids Struct. 40 (2003) 343–360. https://doi.org/10.1016/S0020-7683(02)00526-7.

[66] R. Shu, L. Tang, T. Yin, High-temperature effect on the physical and dynamic compressive properties of pre-stressed cement mortar, J. Adv. Concr. Technol. 17 (2019) 232–243. https://doi.org/10.3151/jact.17.5.232.

[67] J. Xiao, L. Li, L. Shen, C.S. Poon, Compressive behaviour of recycled aggregate concrete under impact loading, Cem. Concr. Resea. 71 (2015) 46–55. https://doi.org/10.1016/j.cemconres.2015.01.014.

[68] FIB Model Code for Concrete Structures 2010, Comite Euro-Inernational Du Beton, 2013.

[69] CEB-FIP Model Code 1990 : design code, Comite Euro-Inernational Du Beton, 1990.

[70] H.W. Noh, V.D. Truong, J.Y. Cho, D.J. Kim, Dynamic increase factors for fiber-reinforced cement composites: A review, J. Build. Eng. 56 (2022) 104769. https://doi.org/10.1016/j.jobe.2022.104769.

[71] K.Q. Yu, Y. Ding, Y.X. Zhang, Size effects on tensile properties and compressive strength of engineered cementitious composites, Cem. Concr. Compos. 113 (2020) 103691.

https://doi.org/10.1016/j.cemconcomp.2020.103691.

[72] Z.T. Chen, Y.Z. Yang, Y. Yan, Quasi-static and dynamic compressive mechanical properties of engineered cementitious composite incorporating ground granulated blast furnace slag, Mater. Des. 44 (2013) 500–508. https://doi.org/10.1016/j.matdes.2012.08.037.

[73] M.D. Magalhaes, R.D. Toledo, E.D.R. Fairbairn, Thermal stability of PVA fiber strain hardening cement-based composites, Constr. Build. Mater. 94 (2015) 437–447. https://doi.org/10.1016/j.conbuildmat.2015.07.039.

[74] J. Xiao, Z. Li, Q. Xie, L. Shen, Effect of strain rate on compressive behaviour of high-strength concrete after exposure to elevated temperatures, Fire Saf. J. 83 (2016) 25–37. https://doi.org/10.1016/j.firesaf.2016.04.006.

[75] H. Su, J. Xu, W. Ren, Experimental study on the dynamic compressive mechanical properties of concrete at elevated temperature, Mater. Des. 56 (2014) 579–588. https://doi.org/10.1016/j.matdes.2013.11.024.

[76] S. Rawat, C.K. Lee, Y.X. Zhang, Performance of fibre-reinforced cementitious composites at elevated temperatures: A review, Constr. Build. Mater. 292 (2021) 123382. https://doi.org/10.1016/j.conbuildmat.2021.123382.

[77] Y.N. Chan, X. Luo, W. Sun, Compressive strength and pore structure of high-performance concrete after exposure to high temperature up to 800°C, Cem. Concr. Resea. 30 (2000) 247–251. https://doi.org/10.1016/S0008-8846(99)00240-9.

[78] J.C. Liu, K.H. Tan, S.X. Fan, Residual mechanical properties and spalling resistance of strain-hardening cementitious composite with Class C fly ash, Constr. Build. Mater. 181 (2018) 253–265. https://doi.org/10.1016/j.conbuildmat.2018.06.009.

[79] T. Zhang, Y. Zhang, H. Zhu, Z. Yan, Characterizing the thermal properties of hybrid polypropylene-steel fiber reinforced concrete under heat exposure: Insights into fiber geometry and orientation distribution, Compos. Struct. 275 (2021) 114457. https://doi.org/10.1016/j.compstruct.2021.114457.

[80] D. Li, D. Niu, Q. Fu, D. Luo, Fractal characteristics of pore structure of hybrid Basalt – Polypropylene fibre-reinforced concrete, Cem. Concr. Compos. 109 (2020) 103555. https://doi.org/10.1016/j.cemconcomp.2020.103555.

[81] Q. Zeng, K. Li, T. Fen-Chong, P. Dangla, Pore structure characterization of cement pastes blended with high-volume fly-ash, Cem. Concr. Res. 42 (2012) 194–204.

https://doi.org/10.1016/j.cemconres.2011.09.012.

[82] J. Kim, Y.C. Choi, S. Choi, Fractal Characteristics of Pore Structures in GGBFS-based Cement Pastes, Appl. Surf. Sci. 428 (2018) 304–314. https://doi.org/10.1016/j.apsusc.2017.09.165.

[83] B. Zhang, S. Li, Determination of the Surface Fractal Dimension for Porous Media by Mercury Porosimetry, Ind. Eng. Chem. Res. 34 (1995) 1383–1386. https://doi.org/10.1021/ie00043a044.

[84] Q. Fu, W. Xu, D. Li, N. Li, D. Niu, L. Zhang, B. Guo, Y. Zhang, Dynamic compressive behaviour of hybrid basalt-polypropylene fibre-reinforced concrete under confining pressure: Experimental characterisation and strength criterion, Cem. Concr. Compos. 118 (2021) 103954. https://doi.org/10.1016/j.cemconcomp.2021.103954.

[85] G. Hong, S. Oh, J. Kim, W.J. Chin, Y.J. Kim, S. Choi, C. Song, Surface-fractal-dimension characteristics of cementitious composites with multi-walled carbon nanotubes dispersed by silica fume, Constr. Build. Mater. 329 (2022) 127182. https://doi.org/10.1016/j.conbuildmat.2022.127182.

[86] S.S. Jin, J.X. Zhang, C.Z. Chen, W.L. Chen, Study of Pore Fractal Characteristic of Cement Mortar, J. Build. Mater. 14 (2011) 92-97+105. https://doi.org/10.3969/j.issn.1007-9629.2011.01.019.

[87] H. Zhong, M. Chen, M. Zhang, Engineering properties of sustainable engineered cementitious composites with recycled tyre polymer fibres, Constr. Build. Mater. 370 (2023) 130672. https://doi.org/10.1016/j.conbuildmat.2023.130672.

[88] X. Zhao, S.L. Xu, Q.H. Li, B.K. Chen, Coupled effects of high temperature and strain rate on compressive properties of hybrid fiber UHTCC, Mater. Struct. 52 (2019). https://doi.org/10.1617/s11527-019-1391-4.